Title:

A Bottom-up Volume Reconstruction Method for Atom Probe Tomography

Brief title:

Bottom-up Volume Reconstruction Method

Authors:

Yu-Ting Ling[1,*], Siegfried Cools[2], Janusz Bogdanowicz[3], Claudia Fleischmann[3], Jan De Beenhouwer[1], Jan Sijbers[1] and Wilfried Vandervorst[3,4]

Affiliations:

[1] Imec Vision Lab, University of Antwerp, Universiteitsplein 1, 2610 Antwerp, Belgium

[2] Applied Mathematics Group, University of Antwerp, Middelheimlaan 1, 2020 Antwerp, Belgium

[3] Imec vzw, Kapeldreef 75, 3001 Heverlee, Belgium

[4] Quantum Solid-State Physics, KU Leuven, Celestijnenlaan 200D, 3001 Leuven, Belgium

Corresponding Author:

[*] E-mail address: Yu-Ting.Ling@uantwerpen.be (Yu-Ting Ling)

Abstract

This paper describes a reconstruction method for atom probe tomography (APT) based on a bottom-up approach accounting for (i) the final tip morphology (which is frequently induced by inhomogeneous evaporation probabilities across the tip surface due to laser absorption, heat diffusion effects, and inhomogeneous material properties), (ii) the limited (and changing) field of view, and (iii) the detector efficiency. The reconstruction starts from the final tip morphology and reverses the evaporation sequence through the pseudo-deposition of defined small reconstruction volumes, which are then stacked together to create the full three-dimensional (3D) tip. The subdivision in small reconstruction volumes allows the scheme to account for the changing tip shape and field of view as evaporation proceeds. Atoms within a small reconstruction volume are reconstructed at once by placing atoms back onto their possible lattice sites through a trajectory-matching process involving simulated and experimental hit maps. As the ejected ion trajectories are simulated using detailed electrostatic modeling inside the chamber, no simplifications have been imposed on the shape of the trajectories, projection laws, or tip surface. We demonstrate the superior performance of our approach over the conventional reconstruction method (Bas) for an asymmetrical tip shape.

Keywords:

Atom probe tomography, Laser, Tip shape evolution, Trajectory-matching, Reconstruction, Simulation

1. Introduction

Atom probe tomography (APT) is a powerful technique which determining the three-dimensional (3D) elemental composition of a sample (Kelly & Larson, 2012; Miller & Forbes, 2014). Atoms on the apex of a needle-shaped sample are exposed to a high electric field (several tens of volts per nanometer) and are eventually evaporated in a controlled manner from the surface by applying additional voltage or laser pulses. Atoms that receive sufficient energy to overcome the evaporation barrier leave the surface as ions. Some of them are guided by the electric field distribution toward the position-sensitive detector. Some atoms miss the detector due to its finite size, limiting the field of view (FOV) at the tip apex. Moreover, despite the recent improvements in detector efficiency, only about 50 to 70% of the evaporated atoms within the FOV can be detected (Barnes et al., 2018; Geiser et al., 2007).

Laser-assisted APT (La-APT) is now widely used for all materials, especially for semiconductors or less conductive materials (Giddings et al., 2018; Kambham et al., 2013; Kambham et al., 2011; Martin et al., 2018; Tu et al., 2017), due to its higher success rate and improved mass resolution compared to the voltage mode APT (Blavette et al., 2010; Kelly et al., 2014). In this case, the evaporation probabilities of the atoms are enhanced by a temporary increase in thermal energy linked to the duration of the laser pulse (Bogdanowicz et al., 2013; Houard et al., 2010; Koelling et al., 2013; Vella, 2013). One of the critical side effects of using of a laser in La-APT is that uneven heating may occur because the laser light does not uniformly illuminate the tip apex (Bogdanowicz et al., 2013; Houard et al., 2010; Koelling et al., 2013; Vella, 2013). The details of the absorption pattern also depend on the wavelength of the laser (Bogdanowicz et al., 2013). In the case of commonly used ultraviolet (UV) light, strong one-sided absorption occurs, leading (e.g., in semiconductor tips) to highly asymmetrical tip shapes, as observed using scanning electron microscopy (SEM) (Koelling et al., 2011) and atomic force microscopy (AFM) (Fleischmann et al., 2018). However, in optimum cases, a nearly atomic resolution can still be achieved by applying suitable reconstruction methods (Geiser et al., 2007; Kelly et al., 2014; Vurpillot et al., 2013).

Conventional reconstruction methods, which typically originate from the Bas protocol (Bas et al., 1995), back-project the detected atoms onto the tip by assuming a hemispherical tip shape and a straight flight path from the tip surface to the detector, where the evaporation sequence is used to extract the original location of the atoms along the tip axis. Within this simplified approach (i.e., a hemispherical tip and straight trajectories), the reconstruction is conducted by introducing empirical parameters, such as the image compression factor (ξ) and the field factor (k_f). These parameters are sensitive to the surface and tip geometry (e.g., the tip radius, shank angle, etc.), may vary during the evaporation process (Gault et al., 2011; Hatzoglou et al., 2019), and are difficult to be obtained directly. Hence, the quantification of these parameters frequently relies on intense calibration efforts. The reconstructed volume of a tip is limited to the FOV area and does not cover the entire evaporated region. This volume is derived by summarizing the atomic volume for all detected atoms with an artificial scaling to a fixed detection efficiency value. The incorrect estimation of the detection efficiency or imperfect calibration of reconstruction parameters leads to reconstruction artifacts. Other artifacts may be induced while reconstructing tips with inhomogeneous materials or asymmetric tips (also FOV) under laser illumination.

The artifacts caused by these assumptions can be minimized if some prior knowledge of the sample is provided. Reconstruction parameters are dynamically optimized to match the reconstructed results according to the known features of the sample, such as its geometrical morphology acquired from imaging techniques like transmission electron microscopy (TEM) or SEM, the distance between lattice planes, the shank angle, the tip radius (Gault et al., 2011; Gault et al., 2009; Hatzoglou et al., 2019; Larson et al., 2013; Larson et al., 2012; Lefebvre et al., 2015; Zschiesche et al., 2019), and clusters or grain boundaries (Baik et al., 2018; Kolli, 2018; Mouton et al., 2017). Corrections to the local magnification are also exploited to eliminate trajectory aberrations that cause low-density poles on the hit maps (Larson et al., 2011). These approaches led to a significant improvement in reconstruction accuracy. However, the reconstruction models are still restricted to samples with axial symmetry.

Simulations can provide more insight into evaporation behaviors, the evolution of tip shapes, and the ion trajectories to provide accurate empirical parameters to address the inhomogeneous and nonaxial symmetrical issues. Some simulations link the reconstruction parameters to the geometric settings of a tip (Gault et al., 2011) and the supporting region (Loi et al., 2013). An analytical model was recently presented to predict the non-hemispherical change in a tip surface for multilayer structures (Rolland et al., 2015a; Rolland et al., 2017). The level set models (Fletcher et al., 2019; Haley et al., 2013; Xu et al., 2015) and the mesoscopic model (Hatzoglou & Vurpillot, 2019) have been developed to describe the evolution of a non-axial symmetrical tip for inhomogeneous materials. Atomistic simulations (Oberdorfer et al., 2013; Oberdorfer & Schmitz, 2011; Vurpillot et al., 1999) were also built to simulate the tip evaporation process and correlate the emission positions to impact positions. The local field variation due to the geometry change can be accounted for via atomic simulations (Kühbach et al., 2019; Oberdorfer et al., 2013; Rolland et al., 2015b). Most of the approaches provide useful guidelines for improving the reconstructions. However, a straightforward reconstruction algorithm is still needed. A radial correction to the magnification was recently developed for reconstructions of inhomogeneous materials (Beinke & Schmitz, 2018), but it is still restricted to axial symmetry. A trajectory-based reconstruction is demonstrated by correlating the trajectories of the forward evaporation with the prior knowledge of the materials using electron tomography (Fletcher et al., 2020). This method is a possible candidate for solving the inhomogeneous materials and non-axial symmetrical issues simultaneously. However, the method is hampered by cases where features are invisible in electron tomography, and the laser effect has not yet been considered.

Thus far, only a few simulators can predict the evolution of a tip and ion trajectory for more general cases of asymmetrical or arbitrarily shaped tips. Among them are 3D electric field simulator TAPSim (Oberdorfer et al., 2013; Oberdorfer & Schmitz, 2011) and the mesh-free Robin-Rolland method (Rolland et al., 2015b). Recently, a bottom-up method was developed by Beinke (Beinke et al., 2016) based on TAPSim, in which the tip was reconstructed with a trajectory-matching technique. The algorithm searches for the closest match between the hitting position on the detector of a detected atom and the simulated hitting positions of the atoms on the surface of the known lattice. This match establishes a one-to-one correlation between the experimentally observed hit position and a launch site on the tip surface and allows the repositioning of the atom at this launch position on the tip surface. Because this bottom-up method deposits the reconstructed atom on the known tip surface, a new known geometry is created to be used for the trajectory calculations for the next atom. The challenges, which are not yet addressed, are how to fill the empty volumes of atoms not detected due to limited detection efficiency and how to recover undetected atoms evaporated from the positions outside the FOV. Incorporating these atoms into the bottom-up reconstruction is crucial for accuracy, as the electrostatic calculations rely on the entire tip geometry. Moreover, because the model does not consider the influence of the evaporation sequence on ion trajectories and all reference lattice positions in one monolayer are compared at once, a geometry change along the reconstruction depth is difficult to capture. Finally, the uneven heating effect of a laser-illuminated tip is currently not considered.

This article expands on this approach and describes a bottom-up reconstruction method, including laser-enhanced evaporation, by integrating an evaporation rate model and modified trajectory-matching model into TAPSim. Instead of reconstructing atoms one by one, this method reconstructs a group of atoms in a small reconstruction volume all at once and stacks different reconstruction volumes into the final 3D volume. The model starts from a known tip geometry and adds a few (virtual) atomic layers. The evaporation sequence and trajectories toward the corresponding hit map positions can be simulated based on the calibrated evaporation model. According to the evaporation sequence, some deposited atoms are sacrificed (e.g., not included as candidate lattice positions for atom reconstruction), and the remaining atoms of the deposited layers define the volume to be reconstructed (e.g., a small volume). To avoid considering complicated laser-tip interactions (absorption patterns and efficiency) and heat redistribution processes (e.g., causing delayed evaporation), the thermal effect of a laser is simplified by including an inhomogeneous distribution of the temperature in the simulations representing a laser-illuminated tip, and an asymmetrical tip shape is formed. The trajectory-matching model is based on an accurate trajectory calculation by solving the Poisson equation at every step and correctly accounting for the electrostatics and field lines generated by an arbitrary tip shape. By comparing the experimental hitting positions with the simulated ones, each detected atom can be aligned to the closest (simulated) hitting position and its launch position. This matching process also compares the evaporation sequences and evaporation rate between the experimental and simulated data which identifies the number of missing atoms, their locations (remaining empty places in the reconstructed volume), and the number of atoms evaporated outside the FOV. In this way, the detector efficiencies and FOV effects are considered. We present this approach by reconstructing crystalline silicon (Si) tips using simulated data sets acquired in voltage and laser mode with various detection efficiencies. The results are compared to the conventional reconstruction approach (Bas).

2. Models

2.1. Reconstruction Method

The proposed bottom-up volume reconstruction method relies on sequentially reconstructing a small piece of the tip volume. By adding the results of consecutively reconstructed small volumes, the entire tip volume is reconstructed. Because the electric field and trajectory path are sensitive to the tip shape's local geometry and the detailed atom distribution on the tip surface, the reconstruction sequence is reversed to the detection sequence (i.e., the last detected atoms are the first to be reconstructed). The starting point is the final tip surface after the last atom was collected, upon which the atoms are placed back. This surface can be obtained by synthesizing 2D images of SEM or TEM from different acquisition angles or directly measuring using 3D AFM quantitatively. As the reconstruction proceeds by positioning the latest evaporated atoms on the tip surface, the tip shape, although changing throughout the reconstruction, remains known. Hence, at every iteration step, the 3D electric field distribution can be calculated based on the shape, allowing an accurate prediction of ion trajectories and hit maps.

To reconstruct this small volume, we rely on evaporation simulations to obtain the number of pulses required to evaporate all atoms inside the volume (also those outside the FOV) and the simulated trajectories with their (eventual) hitting positions on the detector. These simulated data are compared to the experimentally detected evaporation fluxes, sequences, and hit maps. By identifying the closest simulated hitting position for each detected atom, we can define its most probable emission point (trajectory-matching) and place it back to the corresponding lattice site in the reconstruction volume. Because the electrical field distribution and ion trajectories are calculated based on the instantaneously detailed tip shape, no assumption needs to be made regarding projection laws, the field factor, the image compression factor, or tip shape. The same process applies to symmetrical, asymmetrical, and arbitrarily shaped tips.

For example, Fig. 1a to 1f illustrates the reconstruction procedure of a symmetrical tip representing voltage-mode field evaporation. For simplicity, all processes are schematically shown in 2D, although they are performed in 3D simulations. To define the small reconstruction volume at each iteration step, virtual atoms within three nearest neighbor (3NN) lattice distances away from the already known (or final) tip surface are conformally deposited on the top of a tip, as illustrated in Fig. 1a. The deposited lattice structure follows the atomic structure of the known tip, accounting for the constraint imposed by the shank angle. Subsequently, starting from the "new" tip structure, the evaporation process of this volume of virtual atoms is simulated, and the detailed evaporation sequence, number of pulses, and hit maps are predicted. The concept is illustrated in Fig. 1b, where the number within each atom indicates its sequence number.

We assume that the standing voltage remains unchanged during this simulation, which is only justified if the 3NN volume is sufficiently thin. In a real experiment, the curvature of the upper surface of the reconstruction volume may not be the same shape as the known tip surface that we enforced. Therefore, although the simulation performs the evaporation of the entire 3NN volume, atoms from the third layer (pink-colored sacrificial atoms) are only used to generate a more realistic tip shape for accurate electrostatics in the underlying layers and are not used during reconstruction. In this paper, they are referred to as sacrificial atoms. Only atoms from the second and first layers (colored green) are considered (labeled as candidate atoms). As we proceed with the reconstruction from the bottom up, the process stops when an atom from the third layer is elected during the trajectory-matching process (e.g., atom number 12 in Fig. 1b). Figure 1c schematically demonstrates the evaporation sequence of the virtual atoms from the simulation and detected sequence of ions from the experiment. If the evaporation frequency of the deposited material is known (see the evaporation model in Section 2.3), the number of pulses required to remove the virtual atoms from the entire tip is obtained. In the case of a well-calibrated evaporation frequency, the experiment requires an equal number of pulses to the simulation and generates the same number of atoms.

However, less number of atoms is effectively detected because some are generated outside the FOV, whereas some are undetected. The difference between the number of evaporated and detected atoms defines the number of missing atoms. Each detected ion's hit position is investigated to determine the closest hit position on the simulated hit map and the most emission probable point to link the candidate atoms with the experimental data (Fig. 1d). The corresponding candidate atom is then labeled as detected and is replaced by the experimental one. Hence, those atoms are placed back into the lattice sites in the reconstruction volume, as shown in Fig. 1e. The process continues until one of the atoms belonging to the surface (third) layer of the virtual atoms is selected. Then, the search process stops and the remaining empty positions (inside and outside the FOV) in the lattice are filled with substrate atoms. This outcome implies that the present algorithm is only suited to reconstruct diluted systems (i.e., monophase materials without microstructures) with a random distribution of the solute (e.g., doped semiconductors). For a compound, the filling algorithm would need to be more complex to maintain the stoichiometry of the compound. The small volume, including all detected atoms and missing atoms, is completely reconstructed and becomes part of the tip for the next iteration, as illustrated in Fig. 1f. Processes (a) to (e) in Fig. 1 are repeated until all detected atoms are reconstructed.

2.2. Computing the Electric Field

Because evaporation is a process driven by the electric field, the evaporation sequence of small volumes relies on an accurate field distribution simulation. We used the 3D simulation package TAPSim to calculate the electric field. This simulator enables a calculation with sufficient precision on all relevant scales, covering more than seven orders of magnitude because the atomic structure of the tip, the centimeter-sized detector and, analysis chamber must be accommodated. Within this simulation approach, the atom with the highest evaporation probability is selected as the atom to be evaporated. Subsequently, the trajectory path of the selected atom is computed using Newton's equation of motion. The fourth-order Runge-Kutta method is conducted as the integrator for numerically solving the formula (Oberdorfer & Schmitz, 2011). Once the atom is removed from the tip surface, the above procedure is repeated for the subsequent evaporation, considering the changes in tip geometry and electrostatics.

The electric field distribution can be calculated from the distribution of the electrical potential distribution obtained by solving Poisson's equation in a meshed system. For this purpose, a cylindrically shaped domain is employed. Point clouds of atom positions of the tip are defined and placed on the bottom center of the cylinder. The detector is defined on the top of the cylinder with several nodes on it. Supporting nodes in the space are also generated using the distances between nodes that increase gradually from the tip to the detector. Tetrahedral meshes are constructed using Delaunay tessellation with the nodes lying on the corner of each mesh. For better flexibility for an arbitrarily shaped tip and material properties between nodes, the Voronoi tessellation is also computed from Delaunay meshes. All meshes are generated once and remain the same throughout the entire simulation. For each atom that is evaporated, only the label of that atom in the simulator is changed (i.e., from the type of tip material to the vacuum type), which minimizes the effort of creating new meshes and moving boundaries.

Voronoi meshes enable the discretization of Poisson's equation based on the integrated finite difference method (Oberdorfer et al., 2013) where the potential of a selected Voronoi cell φ_i is correlated to the potential of the neighbors φ_j, as shown in Equation (1):

$$\varphi_i = \frac{\frac{\rho_i}{\varepsilon_0}\|V_i\| + \sum_{j \neq i} \gamma_{ij} \varphi_j}{\sum_{j \neq i} \gamma_{ij}} \quad , \qquad (1)$$

where ε_0 is the vacuum permittivity, and ρ_i and V_i are the charge density and mesh volume of the local Voronoi cell, respectively. The coupling factor γ_{ij} is a constant associated with the distance, interface area, and electrical properties between adjacent meshes. Oberdorfer (Oberdorfer et al., 2013) described the detailed derivation.

Iterative methods (Saad, 2003) are commonly used to solve a linear problem to avoid expensive computation time and storage of a large system matrix, as the format is $A\boldsymbol{\varphi} = \boldsymbol{b}$. This method simplifies heavy computations into small tasks of matrix to vector multiplications. The iteration method continuously improves the approximate solution until the difference between the approximate solutions from two consecutive iterations becomes smaller than a predefined tolerance value, signaling convergence. We first employed Jacobi's method, a simple stationary iterative method commonly used in solving linear problems. The electric potential of a selected node i for the new iteration step $k+1$ is represented as φ_i^{k+1}, as follows:

$$\varphi_i^{k+1} = \frac{b_i - \sum_{j \neq i} a_{ij} \varphi_j^k}{a_{ij(j=i)}} \quad , \qquad (2)$$

where b_i is the value of the vector on the right-hand side of the linear equation, and a_{ij} is the ijth element of the sparse matrix A. By comparing Equations (1) and (2), we have the values following on the right-hand side:

$$b_i = \begin{cases} \frac{\rho_i}{\varepsilon_0} \|V_i\| \\ 0 \ \ or \ V_{apply} \ \ (\ i \ is \ Dirichlet\ ) \end{cases} \quad . \qquad (3)$$

The following are diagonal elements of matrix A and the residual elements, respectively:

$$a_{ij(j=i)} = \begin{cases} \sum_{j \neq i} \gamma_{ij} \\ 1 \qquad (\ i \ is \ Dirichlet\ ) \end{cases} \quad , \qquad (4)$$

$$a_{ij(j \neq i)} = \begin{cases} -\gamma_{ij} \\ 0 \qquad (\ i \ is \ Dirichlet\ ) \end{cases} \quad . \qquad (5)$$

Dirichlet boundary conditions are applied for the detector nodes and the tip, where the potential is fixed at zero for the detector and is a constant value (i.e., the applied bias) for the tip. A Neumann boundary condition is used for the bottom nodes between the tip and the cylinder sidewall, which assumes no potential flux across the boundary. This condition provides an equivalent condition of having an infinite tip without severe field interference from the support components of the tip. Elements of the Neumann nodes are treated as standard nodes, and no further modifications are required.

The atomic-scale simulation recalculates the potential after every evaporated atom, which must be done more than a million times to simulate a real tip. Therefore, reducing the computational time is essential, which is commonly achieved through parallelization techniques or by improving the solver efficiency.

The computational process consists of iteratively multiplying the matrix to the vectors; thus, one can solve the sparse matrix system using Krylov subspace methods (Saad, 2003; Shewchuk, 1994). The subspace method projects the problem onto space spanned by the residuals $r_i = b_i - A\varphi_i$, which defines the deviation of the approximated potential and the approaching direction to the actual solution for the next iteration. The conjugate gradient (CG) method (Hestenes & Stiefel, 1952) provides an efficient method of defining a solution that minimizes the residuals in each iteration, significantly reducing the number of iteration cycles compared to non-Krylov methods.

The CG method requires a symmetric and positive definite matrix. For most of the standard nodes where the neighboring nodes are not a part of the boundary, they share the same value of the coupling factor as their neighbors $\gamma_{ij} = \gamma_{ji}$. Hence, matrix A is symmetrical (i.e., $a_{ij} = a_{ji}$). However, for the nodes adjacent to the Dirichlet boundary nodes (i.e., i is standard or Neumann but j is Dirichlet), a_{ij} and b_i must be modified as follows:

$$a_{ij(j=D)} = 0 \quad \text{, and} \qquad (6)$$

$$b_i = \frac{\rho_i}{\varepsilon_0} \|V_i\| + \sum_{j=D} \gamma_{ij} \varphi_j \quad . \qquad (7)$$

The CG method may suffer from poor convergence if it is not conditioned well. With proper preconditioning, CG is considered a method that improves the convergence rate (Ghysels & Vanroose, 2014; Saad, 2003). Therefore, in our simulation, a diagonal preconditioner is tested.

In this article, the computational time between Jacobi's method and the preconditioned CG method is compared.

2.3. Evaporation Model

In this section, an evaporation model is developed to consider the field and thermal effects. However, our model does not include actual voltage or laser pulses, unlike the pulse model (Vurpillot et al., 2009). To avoid most of the unknown mechanism and uncertainties of actual pulses, we used the evaporation frequency as an alternative method to represent the evaporation behaviors under pulses effectively. The evaporation frequency is defined as the number of atoms evaporated in a unit period. The model is calibrated to the detection flux from real experimental data; thus, the simulation time can be aligned with the real time. This time alignment enables the direct comparison between the simulated evaporation sequence and the detected sequence, allowing for identifying of the missing atoms. The pulsing frequency is a known factor; therefore, the evaporation frequency unit is interchangeable between the number of atoms per second and the number of atoms per pulse.

2.3.1 Calibrating the evaporation model to the experimental data

The evaporation frequency ν (s^{-1}), represents the probability of evaporation of an atom on the tip surface, which can be described by the rate equation in Arrhenius format (Miller & Forbes, 2014):

$$\nu = \nu_0 \cdot exp(-\frac{Q_b(F)}{k_B T_{local}}) \quad , \qquad (8)$$

where ν_0 denotes the pre-exponential factor of the evaporation rate constant, F is the strength of the electric field, Q_b is the evaporation barrier for field evaporation, k_B is the Boltzmann constant and T_{local} is the local temperature of the atom.

The detection flux represents the number of atoms collected by the detector in a unit period. The detection flux is correlated to the approximated evaporation frequency of atoms on the exposed tip surface as follows:

$$R_{det} = n_s \eta \nu \quad , \qquad (9)$$

where n_s represents the number of atoms on the tip surface in the FOV, and η is the detection efficiency. The detection efficiency is a constant for the APT tool, whereas the number of surface atoms in the FOV could vary with the applied bias and tip geometry. However, in the specific situation in which the geometry and field changes are negligible, the number of surface atoms can be assumed to be constant; thus, the pre-exponential factor and evaporation barrier in Equation (8) can be deduced from the detection flux.

Figure 2a illustrates the detection flux of a voltage evaporated Si tip measured by Thompson (Thompson et al., 2007). The significant increase in the detected flux beyond the applied biases of about 4.5 kV, marks the transition between the evaporation mechanism for low and high fields. In the low-field region, evaporation is dominated by hydrogen-assisted Si evaporation as indicated by hydrogen signals in the mass-to-charge spectrum, while the high-field region is dominated by Si self-evaporation. The evaporation at temperatures lower than 110 K could involve an ion tunneling process and becomes insensitive to the temperature, similar to the observed tunneling effect of dopant atoms (Menand & Kingham, 1984, 1985).

For each data point in Fig. 2a, 10,000 atoms were collected. The geometrical and field changes for a large tip are ignored in the acquisition period because only a few atomic layers are evaporated over a commonly used tip size (tip radius > 30 nm), implying a constant number of surface atoms $\mathrm{n_s}$ in the FOV. In this condition, the field-dependent activation energy of different evaporation mechanisms can be extracted separately from Arrhenius plots. The activation energy for hydrogen assisted Si evaporation in the low bias region between 2 and 4.5 kV ranges from 0.218 to 0.15 eV. For Si self-evaporation in the high bias region from 4.5

to 10 kV, these values range from 0.56 to 0.78 eV. The activation energy for a full-bias region from 2 to 10 kV ranges from 0.001 to 0.005 eV for the tunneling mechanism. Extracted prefactors and activation energy as a function of applied bias for different evaporation mechanisms are fitted by empirical equations, represented in Table 1. The prefactors and activation energy are all field-dependent, which is similar to Tungsten data found by Kellogg (Kellogg, 1984).

According to the extracted data in Table 1, the evaporation frequency of each evaporation mechanism can be derived by excluding the constant detection efficiency η and surface atoms $\mathrm{n_s}$ from the flux based on Equations (8) and (9). For the deduced evaporation frequencies, ν_{H-Si} represents the hydrogen-assisted Si evaporation, ν_{Si} describes the pure Si evaporation and ν_{tunnel} is the tunneling mechanism. Notably, in our simulations, a hybrid system is necessary to capture the behavior over the full range of the applied voltages, as shown in Equations (10) and (11):

$$\nu_{total} = \nu_{H-Si} + \nu_{tunnel} \ , \quad for\, V \ \leq 4.5\, kV \quad , \qquad (10)$$

$$\nu_{total} = \nu_{Si} + \nu_{tunnel} \ , \quad for\, V \ > 4.5\, kV \quad , \qquad (11)$$

Hence, the total evaporation frequency for a bias lower than 4.5 kV is defined as being due to the combined effect of the hydrogen-assisted Si evaporation and tunneling. In contrast, the evaporation frequency for higher biases is the sum of the Si self-evaporation and tunneling process.

The fitting quality of the model is proven by good alignments between the calculated fluxes from the hybrid model (lines) and detected fluxes from the experiment (symbols) for various temperature (see Fig. 2a.). The experimental values were obtained at temperatures equal to or higher than 90 K; however, we extended the model calculations to the more commonly used temperature of 50 K.

2.3.2 Calculating evaporation frequency for surface atoms

The evaporation frequency of every exposed atom must be provided to simulate the emission of an atom in an atomic model. The evaporation frequency at a fixed temperature is a process driven by electric field; thus, the extracted pre-exponential factor and activation energy Q_b, which were originally formulated as a function of the applied bias, are rewritten via the simple relationship $F = V/f_{scale}$, where f_{scale} is a geometric scaling parameter. In line with the negligible geometrical change in the tip surface, f_{scale} can be treated as a constant value. Therefore, the evaporation frequency as a function of the electric field is deduced, as illustrated in Fig. 2b.

Considering the omnipresent use of laser assisted evaporation with semiconductors and its substantial role in tip shapes, we considered it essential to add the concept of a temperature distribution across the tip apex in the simulator. To demonstrate the effect of such temperature gradients and our ability to deal with the resulting asymmetrical tip shapes, we introduced an arbitrary yet simplistic description of a temperature distribution, which currently has no direct detailed physical justification. Its description can easily be modified into a more precise description of the laser-tip interaction if the latter becomes available. In our simulation, the tip is divided into several long voxels with a small area on the illuminating surface and a full length across the tip width. By assuming that the temperature redistribution does not lead to a complete thermalization within the duration of a laser pulse, the temperature of each voxel is calculated independently by considering a heat source operative on the surface (such as a localized area illuminated by a laser beam).

Therefore, the temperature distribution (in a voxel) is described in 1D by a predefined arbitrary temperature T_{Laser} on the illuminated surface. The temperature across the tip apex decreases with the distance dx away from the illuminated surface following an exponential decay function:

$$T(dx) = T_{Base} + (T_{Laser} - T_{Base}) \cdot exp(-\frac{dx}{\lambda}) \quad , \qquad (12)$$

where λ denotes the decay length. Again, this is an extremely simplistic description that can later be modified to a truly 3D distribution when refinements related to the laser absorption process, heat diffusion, and cooling process are better understood and modelled.

2.3.3 Testing the evaporation model

Tip shapes created under voltage or laser-assisted evaporation conditions are simulated to validate the evaporation model. Single crystalline <001> Si tips are employed for the simulations, which, as a starting point, assume a hemispherical cap on top of a truncated cone with an apex radius of 20 nm, tip height of 50 nm, and a half shank angle of 8°. A constant bias of 4 kV is applied at the bottom of the tip. For all cases, the base temperature T_{Base} is set at 50 K, whereas the surface temperature on the illuminated side, T_{Laser}, is set at a fixed value of 120 K with a decay length equal to 100 nm for laser cases.

The simulated results (i.e., the tip shapes before and after evaporation and the corresponding hit maps) for the voltage and laser mode are depicted in Fig. 3a and 3b, respectively. In the voltage evaporation case (Fig. 3a), the temperature is homogeneous throughout the tip; thus, the electric field strength dominates the evaporation sequence. Atoms at the apex experience a higher electric field than those on the cone sidewall; thus, protruding atoms on the exposed surface have the highest probability of evaporation. Therefore, the tip surface is polished by the field and a surface with a nearly equivalent evaporation probability is formed, leading to a symmetrical and nearly hemispherical tip shape.

In the laser-assisted case (Fig. 3b), the evaporation probability across the tip is influenced by the nonuniform temperature distribution. Initially, the evaporation probability at the illuminated surface is the highest, as the thermal energy allows the atoms to overcome the evaporation barrier more easily. However, as more atoms at the illuminated surface are increasingly evaporated, the curvature near the apex shrinks. The atoms on the shadow side experience a higher electric field due to an increased curvature, leading to an increase in their evaporation probability. As a result, the apex of the tip gradually shifts toward the shadow side, away from the center axis of the initial tip, leading to an asymmetrical tip shape.

Figure 3c and 3d depicts the simulated desorption hit maps for the voltage and laser cases as viewed by a large virtual detector (400 × 400 mm). The poles and zone lines in the desorption maps result from the microscopic nature of the surface with ring-shaped terraces and facets of the crystal planes in some major directions. Around these lattice planes, the electric field is locally distorted resulting in some trajectory aberrations (Gruber et al., 2011; Kühbach et al., 2019). A voltage-evaporated tip results in a symmetrical map, whereas the laser-evaporated tip shows an asymmetric hit map where the distorted patterns of the poles and zone lines indicate the effect of local differences in magnification. This asymmetric feature is not evident in practice due to the much smaller size of the real detector and limited FOV (circle on the hit map). Only one clear pole and two crossing zone lines of a Si tip are visible.

The geometrical change in a tip during evaporation can be observed by monitoring the cross-sectional slices along the *x*- and *y*-directions, as displayed in Fig. 4. For a voltage case (Fig. 4a), similar results can be observed in both directions, and the symmetrical and quasi-hemispherical tip shape remains during the evaporation processes. In contrast, the laser case results in non-axial asymmetric tip evolutions as observed in the *y*- slice in Fig. 4b. The erosion starts at the illumination side, causing shrinkage in the apex size and a shift in the apex axis toward the shadow side after some evaporation. The tip shape finally saturates into a certain geometry, where steady-state evaporation is reached. The tip surfaces under further evaporation evolve nearly parallel to each other without changing the radius, except the depth. The surfaces in the *x*- slice remain symmetrical because atoms at the cutting plane at $x = 0$ are all exposed to the same laser illumination and experience the same temperature. Despite the simplified rate model and the arbitrary temperature distribution the prediction of the final tip is qualitatively similar to the AFM or TEM images reported for Si-tips evaporated in laser mode (Fleischmann et al., 2018; Koelling et al., 2011). A more complex description of the laser and tip interactions are required and elaborate 3D calibrations on real tip shapes are required to match the actual shape of a tip quantitatively.

Thus far, the simulations in Fig. 3 display the hit maps of all evaporated atoms onto an infinite detector. By superimposing the physical size of the real detector (red circle in Fig 3c and 3d) the atoms confined to the FOV region can be identified and are highlighted by the gray areas in Fig. 4a and 4b. In the case of voltage evaporation, the FOV region and the evolving tip shape are symmetrical. The boundary of the FOV region is not aligned to the shank angle of the cone edge but is steeper. For the *y*- slices of the laser case, the extracted FOV region is asymmetrical and no longer stationary at the tip center because of the tilted surface of the tip apex. Even the FOV region remains close to a cylindrical shape in 3D and does not change severely in size. The drift of the FOV region toward the shadow side makes the visualization of the FOV region an inverted trapezoidal shape, as shown by the gray region highlighted in the *x*-slice. These results indicate that assuming a fixed and symmetrical FOV region is not valid for experiments with laser-assisted evaporation.

3. Validation of the Reconstruction Method

3.1. Generation of Data-sets

A straightforward method for validating the accuracy of the reconstruction is to compare the reconstructed atoms to their ideal emission positions. Therefore, we reconstructed data-sets from simulated tips, where the original positions of the atoms were also available. Single crystalline <001> Si tips were used in the simulation and were evaporated in voltage and laser mode, as depicted in Fig. 5a and 5b. The evaporation was performed by removing the atom with the highest evaporation frequency away from the tip surface, like the calibrated model shown in Section 2.3.

A small tip with a tip height of 42 nm, an apex radius of 2 nm, and a half shank angle of 4° was used, and only 5,000 atoms were evaporated. As this is a small tip, even with a low tip bias of 500 V, a high electric field suitable for evaporation was reached. The base temperature was set at 50 K for all cases, but the effect of an additional heat source was included for the laser-assisted case by assigning a surface temperature of 120 K at the illuminated surface, exponentially decreasing away from that position with a decay length of 100 nm. Atoms in the FOV were "detected" by assigning a detector diameter of 10 cm on the hit maps in Fig. 5c and 5d. The simulated desorption sequence, spatial distribution of the ions on hit maps, and duration (interval pulses) between two detected atoms were treated as experimental data and were reconstructed afterward starting from the simulated final tip shape.

In some cases, 50% of the data points were randomly removed from the simulated data set to mimic the actual experimental conditions with limited detection efficiency. The deterministic method of removing the atom with the highest evaporation frequency from the tip surface may not fully reflect the actual laser heating effect in actual experiments, even if the inhomogeneous temperature distribution is implemented. The increase in stochastic changes in the evaporation sequence while increasing the temperature was not considered in the model.

3.2. Reconstruction

We only reconstructed about 4,500 atoms of total evaporations (5,000), as illustrated by the boundaries marked in Fig. 5a and 5b. The atoms near the apex are typically neglected because they are generally part of the start-up process involving tip and laser alignments and removing contamination from the tip surface. For consistency, a deterministic method was also used to select the atom to be removed from the small volume for generating the impact positions for trajectory-matching.

Figure 6a illustrates the final reconstruction results and some small reconstruction volumes in case of voltage evaporation. Around 91% of the atoms from the simulated hit map were restored to their correct emission positions, including the atoms inside and outside the FOV. The overall reconstructed tip exhibits a uniform distribution of Si density. The local aberration effect, which causes a low-density region around zone lines and poles after the reconstruction, was eliminated because of the accurate trajectory-matching process. The differences between the location of the reconstructed atoms relative to their original positions are highlighted by the black lines.

At the beginning of reconstruction (i.e., the bottom of the reconstructed volume), most atoms are positioned well. Only a limited number of misplacements occurs, which increases as placement errors may influence the calculations in higher lying layers (error propagation) by increasing the reconstruction height. Among the potential sources for misplacements, we found that a small number of data points exist for which the same launch position is estimated, which most likely results from an incorrect prediction of the evaporation sequence. Although we sacrificed the third atom layer in each (small) reconstruction volume to compute the Poisson solution, the evaporation sequence still not perfectly aligned with the evaporation sequence while generating data from the demonstrated tip.

The mismatch between the evaporation sequences also translates into errors during the trajectory-matching process, as presented in Fig. 6b. Typically, the number of mismatched atoms can vary between 1.1% and 10.2% of the total atoms in each small volume and originate from atoms being assigned the wrong evaporation sequence number. Therefore, they are not reconstructed in the specific volume they should belong to but are swept into the next volume for reconstruction, causing error propagation in higher volumes. The swept data can still find a position not too far from the ideal position because of the repeated atomic structure in a crystalline material. A similar hit map distribution occurs with only small spatial errors in the x- and y- directions.

Figure 7a presents the reconstruction results for laser illumination. A similar level of distance displacements and migration effects is observed compared to the symmetrical voltage evaporation case. Over 93% of the atoms were accurately reconstructed. This successful reconstruction implies that ions can be reconstructed without the negative influence of the asymmetrical tip shape and the nonconstant, nonsymmetrical FOV effect. The latter is an important characteristic of our novel reconstruction approach.

The y-slices with a width of 0.8 nm at the center of the reconstructed tips are compared to visualize better the differences between our approach and that based on the conventional Bas protocol. The distribution of the averaged displacement error along the reconstruction length is displayed in Fig. 8. The averaged displacement error Δd is defined as the average of the Euclidean distance of the reconstructed atoms to their original positions in a small volume. In the conventional reconstruction method, the image compression and the field factors are carefully chosen to fit the total height of the data tip. However, the averaged error Δd in Fig. 8d continues increasing with the reconstruction length. By analyzing the errors in the vertical direction Δz and the lateral direction Δxy, we observe that the vertical errors remain at the sub-angstrom level, whereas the lateral errors indicate severe distortions. The major errors in the lateral direction come from the misplacement of the atoms, which are forced to fit into a symmetrical tip shape following the basic assumption of the Bas model.

In contrast, the bottom-up method exhibits better reconstruction accuracy and a tighter distribution of the correct atom placements (see Fig. 8b). The averaged errors in Fig. 8d remain at a low level with only a small error propagation from the bottom to the top. As presented in Fig. 8c, no degradation in accuracy occurs when considering various detection efficiencies because the trajectory-matching process is independent of the number of detected atoms.

4. Discussion

The bottom-up reconstruction method discussed above is clearly capable of reconstructing tips evaporated in voltage or laser modes, particularly when the evaporation process leads to an asymmetrical tip shape. The superiority of the bottom-up approach versus the conventional reconstruction becomes apparent. The intrinsic assumption of a hemispherical tip shape and associated simple projection laws breaks down rapidly in such a case, even if a dynamic adjustment of the image compression and field factor is implemented. However, several challenges remain evident when the method is applied to real experiments.

As indicated in Fig 8, one concern is that errors start accumulating due to the bottom-up approach, such that the entire solution might diverge for large reconstructed volumes. At present, we identified two sources for this behavior. One of the possible sources may come from numerical errors. As we heavily rely on the trajectory-matching process, the Poisson solution must be calculated very precisely. The convergence criteria must be stringent to maintain a stable solution and minimal error propagation. Using Jacobi's method, the absolute deviation of the potential between iterations was smaller than 0.1 mV. For calculations using the CG method, the norm of the residual error $\boldsymbol{r_k^T r_k}$ was less than 1×10^{-20}, where $\boldsymbol{r_k}$ represents the residual at the kth iteration.

Moreover, precise calculations of electrostatics depend on how realistically the conditions in a chamber are reproduced in a simulation. Even when a nearly full-scaled simulation domain in TAPSim is used, several items, such as supporting wires, holders, the local electrode and the reflectron are not modeled. Except for those listed above, imperfect factors, such as the misalignment or tilting between the tip and the detector or the local electrode contamination must be monitored.

The other source of error propagation lies in the use of a small reconstruction volume of only 3NN virtual atoms and the restriction of the sacrificial atoms to the third layer of that volume. A larger virtual reconstruction volume connected to more layers of sacrificed virtual atoms results in, a larger tip shape, which is used to estimate the evaporation sequence, and better convergence to the simulated trajectories. Thus far, we explored the deposition of xNN lattices ($x > 3$) for each iteration, as more sacrificial atoms lead to higher computational efforts and decrease the reconstruction efficiency. As the current reconstruction results achieved an accuracy of > 91% and an acceptable displacement errors on the sub-angstrom scales, the 3NN lattices are considered an acceptable choice. Progress in computational speed might lead to revisiting this conclusion.

The computational speed is currently a significant challenge to apply the proposed model in practical applications. Atomistic simulation enables the reconstruction with high resolution, but has the speed limitations. As the potential distribution must be recalculated after the placement of each atom, more than a million calculation cycles are required for reconstructing a real tip. As indicated, the evaporation and trajectory calculations rely on precise calculations of the electric field, such that strict convergence tolerances must be used, increasing the number of iterations while solving the Poisson equation. For small tips with a radius of 2 nm, as used in Fig. 5, the initial speed was about 0.7 atoms/min using Jacobi's iteration method with eight threads in parallel. After some optimizations and changing the solver to the CG method, the simulation speed improved to about 950 atoms/min. However, for a large tip with a radius of 30 nm, the speed still drops to 24 atoms/min due to the increased mesh density. Hence, for real applications, methods for accelerating to around two to three orders of magnitude are still necessary.

Another limitation of the reconstruction method is that the atoms used in the virtual volume (to calculate the tip shape and field distributions) are currently identical and equal to the matrix.

For semiconductor applications, this is not a problem because the prime application is often the analysis of a dilute system (i.e., a bulk material with dopant atoms of less than 1 atomic percentage of all elements), such that the elements and lattice structures of the virtual atoms are essentially the same as those of the experimental data. The placement of the missing atoms, linked to the detection efficiency or FOV, is also possible if we assume that the presence of some dopant atoms has no effect on the overall evaporation rate and sequences.

However, for most of the materials being analyzed in practice, a complex system (e.g., compound, precipitates, or grain boundaries) is involved, and some issues must be addressed. For example, for a compound material, the composition may change throughout the evaporation process. When the reconstruction model is performed, deposited lattices on the tip surface and the evaporation frequency change as a function of the composition must be determined. Additionally, the current model assumes the same deposited material inside and outside the FOV region; thus, it may face a problem using materials with different evaporation frequencies and some part of the material lies outside the FOV. All of which indicates that prior knowledge might be required, such as information on lattice structures or material interfaces.

Several laser heating effects should also be investigated. First, the temperature of an evaporated atom is a critical factor for modeling its evaporation behavior. A relatively simple model is temporarily used in our model to generate an inhomogeneous temperature distribution to mimic the possible temperature distribution in a tip. Future implementation should integrate theoretical calculations and experimental observations for modeling the tip-laser interaction effect to reflect the absorption and dynamic motion for thermal redistribution. Nevertheless, calibrating the modeled temperature to the real temperature of a tip is currently challenging due to the lack of in-time temperature data during laser illumination.

Second, the model should consider the actual conditions of laser pulses. The temperature may thermally accumulate and diffuse as a function of time. Thus, the heating and cooling rates of a laser pulse and the duration time between pulses must be simulated.

Third, the uncertainty of the evaporation sequence should be included, especially at high temperatures. At low temperatures, the evaporation process is dominated by the electric field. Atoms with a higher field evaporated prior to those with low-field atoms on the exposed tip surface, making the evaporation sequence perfectly ordered following the strength of the field. This result can be modeled by defining the evaporated atom as the one with the highest evaporation probability (i.e., a deterministic method). However, at high temperatures, the evaporation probabilities of low-field atoms are thermally increased and close to the values of high field atoms. A compatible level of probabilities between the low-field and high-field atoms causes irregular evaporation sequence. Gruber had proved this phenomenon by introducing the random selection of evaporated atoms based on a kinetic Monte Carlo approach (Gruber et al., 2011). The model also predicted the increments of the lateral displacement of the impact positions as the temperature increased. The displacement is expected to become more severe for low activation energy materials (e.g., hydrogen-assisted Si evaporation in our case). Therefore, if a non-deterministic method of determining atoms for the emission is implemented in this model, the accuracy of the bottom-up reconstruction degrades.

Finally, the surface migration effect is not included in the model. Recently, the migration path of an unstable atom can be traced, as shown in Oberdorfer's article (Oberdorfer et al., 2018). However, the migration effect is a stochastic process, which is almost irreversible, making it hard to reconstruct. Implementing the surface migration effect should merge the current model with molecular dynamic calculations, creating more computational loadings to our system. For these viewpoints, a more efficient and robust method is required to capture all these complicated effects that involve laser heating.

5. Conclusion

In conclusion, a new trajectory-based bottom-up reconstruction method was developed, which applies to reconstructing symmetrical or asymmetrical tips in diluted materials. As the simulation of the tip evaporation forms an important part of the algorithm, we also introduced a temperature effect (in addition to the electric field), such that the current standard process of tip evaporation with laser illumination can be considered. Within this bottom-up approach, the trajectory-matching process allows identifying the launch position of the detected atoms and their reconstruction. Unlike the conventional method, no specific projection laws are used such that arbitrary tip shapes can be reconstructed. An equally important asset of the present implementation is that all missing atoms can be reconstructed without the restriction of the FOV or the detection efficiency. Future work will focus on improving the speed, adding laser heating effects and applications on real tips. The extension to compound materials and, non-crystalline systems and releasing the restriction that the reconstructed atoms are only accepted on lattice sites will also be investigated.

Reference

Baik, S.I., Isheim, D., & Seidman, D.N. (2018). Systematic approaches for targeting an atom-probe tomography sample fabricated in a thin TEM specimen: Correlative structural, chemical and 3-D reconstruction analyses. *Ultramicroscopy,* **184**, 284-292.

Barnes, J., Grenier, A., Mouton, I., Barraud, S., Audoit, G., Bogdanowicz, J., Fleischmann, C., Melkonyan, D., Vandervorst, W., & Duguay, S. (2018). Atom probe tomography for advanced nanoelectronic devices: Current status and perspectives. *Scr Mater,* **148**, 91-97.

Bas, P., Bostel, A., Deconihout, B., & Blavette, D. (1995). A general protocol for the reconstruction of 3D atom probe data. *Appl Surf Sci,* **87**, 298-304.

Beinke, D., Oberdorfer, C., & Schmitz, G. (2016). Towards an accurate volume reconstruction in atom probe tomography. *Ultramicroscopy,* **165**, 34-41.

Beinke, D., & Schmitz, G. (2018). Atom Probe Reconstruction With a Locally Varying Emitter Shape. *Microsc Microanal,* **25**(2), 280-287.

Blavette, D., Cadel, E., Cojocaru-Mirédin, O., & Deconihout, B. (2010). The investigation of boron-doped silicon using atom probe tomography. In *IOP Conference Series: Materials Science and Engineering*, pp. 012004. IOP Publishing.

Bogdanowicz, J., Gilbert, M., Innocenti, N., Koelling, S., Vanderheyden, B., & Vandervorst, W. (2013). Light absorption in conical silicon particles. *Opt Express,* **21**(3), 3891-3896.

Fleischmann, C., Paredis, K., Melkonyan, D., & Vandervorst, W. (2018). Revealing the 3-dimensional shape of atom probe tips by atomic force microscopy. *Ultramicroscopy,* **194**, 221-226.

Fletcher, C., Moody, M.P., & Haley, D. (2019). Fast modelling of field evaporation in atom probe tomography using level set methods. *J Phys D: Appl Phys,* **52**(43), 435305.

Fletcher, C., Moody, M.P., & Haley, D. (2020). Towards model-driven reconstruction in atom probe tomography. *J Phys D: Appl Phys,* **53**(47), 475303.

Gault, B., Haley, D., de Geuser, F., Moody, M.P., Marquis, E.A., Larson, D.J., & Geiser, B.P. (2011). Advances in the reconstruction of atom probe tomography data. *Ultramicroscopy,* **111**(6), 448-457.

Gault, B., Moody, M.P., De Geuser, F., Tsafnat, G., La Fontaine, A., Stephenson, L.T., Haley, D., & Ringer, S.P. (2009). Advances in the calibration of atom probe tomographic reconstruction. *J Appl Phys,* **105**(3), 034913.

Geiser, B.P., Kelly, T.F., Larson, D.J., Jason, S., & P, R.J. (2007). Spatial distribution maps for atom probe tomography. *Microsc Microanal,* **13**, 437-447.

Ghysels, P., & Vanroose, W. (2014). Hiding global synchronization latency in the preconditioned conjugate gradient algorithm. *Parallel Comput,* **40**(7), 224-238.

Giddings, A.D., Koelling, S., Shimizu, Y., Estivill, R., Inoue, K., Vandervorst, W., & Yeoh, W.K. (2018). Industrial application of atom probe tomography to semiconductor devices. *Scr Mater,* **148**, 82-90.

Gruber, M., Vurpillot, F., Bostel, A., & Deconihout, B. (2011). Field evaporation: A kinetic Monte Carlo approach on the influence of temperature. *Surface science,* **605**(23-24), 2025-2031.

Haley, D., Moody, M.P., & Smith, G.D. (2013). Level set methods for modelling field evaporation in atom probe. *Microsc Microanal,* **19**(6), 1709-1717.

Hatzoglou, C., Da Costa, G., & Vurpillot, F. (2019). Enhanced dynamic reconstruction for atom probe tomography. *Ultramicroscopy,* **197**, 72-82.

Hatzoglou, C., & Vurpillot, F. (2019). A Mesoscopic Field Evaporation Model. *Microsc Microanal,* **25**(S2), 286-287.

Hestenes, M.R., & Stiefel, E. (1952). Methods of conjugate gradients for solving linear systems. *J Res Natl Bur Stand,* **49**(6), 409-436.

Houard, J., Vella, A., Vurpillot, F., & Deconihout, B. (2010). Optical near-field absorption at a metal tip far from plasmonic resonance. *Phys Rev B,* **81**(12), 125411.

Kühbach, M., Breen, A., Herbig, M., & Gault, B. (2019). Building a Library of Simulated Atom Probe Data for Different Crystal Structures and Tip Orientations Using TAPSim. *Microsc Microanal,* **25**(2), 320-330.

Kambham, A.K., Kumar, A., Gilbert, M., & Vandervorst, W. (2013). 3D site specific sample preparation and analysis of 3D devices (FinFETs) by atom probe tomography. *Ultramicroscopy,* **132**, 65-69.

Kambham, A.K., Mody, J., Gilbert, M., Koelling, S., & Vandervorst, W. (2011). Atom-probe for FinFET dopant characterization. *Ultramicroscopy,* **111**(6), 535-539.

Kellogg, G.L. (1984). Measurement of activation energies for field evaporation of tungsten ions as a function of electric field. *Phys Rev B,* **29**(8), 4304-4312.

Kelly, T.F., & Larson, D.J. (2012). Atom probe tomography 2012. *Annual review of materials research,* **42**, 1-31.

Kelly, T.F., Vella, A., Bunton, J.H., Houard, J., Silaeva, E.P., Bogdanowicz, J., & Vandervorst, W. (2014). Laser pulsing of field evaporation in atom probe tomography. *Curr Opin Solid State Mater Sci,* **18**(2), 81-89.

Koelling, S., Innocenti, N., Bogdanowicz, J., & Vandervorst, W. (2013). Optimal laser positioning for laser-assisted atom probe tomography. *Ultramicroscopy,* **132**, 70-74.

Koelling, S., Innocenti, N., Schulze, A., Gilbert, M., Kambham, A., & Vandervorst, W. (2011). In-situ observation of non-hemispherical tip shape formation during laser-assisted atom probe tomography. *J Appl Phys,* **109**(10), 104909.

Kolli, R.P. (2018). Atom Probe Tomography: A Review of Correlative Analysis of Interfaces and Precipitates in Metals and Alloys. *JOM,* **70**(9), 1725-1735.

Larson, D.J., Gault, B., Geiser, B.P., De Geuser, F., & Vurpillot, F. (2013). Atom probe tomography spatial reconstruction: Status and directions. *Curr Opin Solid State Mater Sci,* **17**(5), 236-247.

Larson, D.J., Geiser, B.P., Prosa, T.J., Gerstl, S., Reinhard, D.A., & Kelly, T.F. (2011). Improvements in planar feature reconstructions in atom probe tomography. *J Microsc,* **243**(1), 15-30.

Larson, D.J., Geiser, B.P., Prosa, T.J., & Kelly, T.F. (2012). On the use of simulated field-evaporated specimen apex shapes in atom probe tomography data reconstruction. *Microsc Microanal,* **18**(5), 953-963.

Lefebvre, W., Hernandez-Maldonado, D., Moyon, F., Cuvilly, F., Vaudolon, C., Shinde, D., & Vurpillot, F. (2015). HAADF–STEM atom counting in atom probe tomography specimens: Towards quantitative correlative microscopy. *Ultramicroscopy,* **159**, 403-412.

Loi, S.T., Gault, B., Ringer, S.P., Larson, D.J., & Geiser, B.P. (2013). Electrostatic simulations of a local electrode atom probe: The dependence of tomographic reconstruction parameters on specimen and microscope geometry. *Ultramicroscopy,* **132**, 107-113.

Martin, A.J., Wei, Y., & Scholze, A. (2018). Analyzing the channel dopant profile in next-generation FinFETs via atom probe tomography. *Ultramicroscopy,* **186**, 104-111.

Menand, A., & Kingham, D.R. (1984). Isotopic variations in field evaporation charge-state of boron ions. *J Phys D: Appl Phys,* **17**(1), 203-208.

Menand, A., & Kingham, D.R. (1985). Evidence for the quantum mechanical tunnelling of boron ions. *J Phys C: Solid State Phys,* **18**(23), 4539-4547.

Miller, M., & Forbes, R. (2014). *Atom-Probe Tomography: The Local Electrode Atom Probe*: Springer US.

Mouton, I., Printemps, T., Grenier, A., Gambacorti, N., Pinna, E., Tiddia, M., Vacca, A., & Mula, G. (2017). Toward an accurate quantification in atom probe tomography reconstruction by correlative electron tomography approach on nanoporous materials. *Ultramicroscopy,* **182**, 112-117.

Oberdorfer, C., Eich, S.M., & Schmitz, G. (2013). A full-scale simulation approach for atom probe tomography. *Ultramicroscopy,* **128**, 55-67.

Oberdorfer, C., & Schmitz, G. (2011). On the field evaporation behavior of dielectric materials in three-dimensional atom probe: a numeric simulation. *Microsc Microanal,* **17**(1), 15-25.

Oberdorfer, C., Withrow, T., Yu, L.J., Fisher, K., Marquis, E.A., & Windl, W. (2018). Influence of surface relaxation on solute atoms positioning within atom probe tomography reconstructions. *Materials Characterization,* **146**, 324-335.

Rolland, N., Larson, D.J., Geiser, B.P., Duguay, S., Vurpillot, F., & Blavette, D. (2015a). An analytical model accounting for tip shape evolution during atom probe analysis of heterogeneous materials. *Ultramicroscopy,* **159**, 195-201.

Rolland, N., Vurpillot, F., Duguay, S., & Blavette, D. (2015b). A meshless algorithm to model field evaporation in atom probe tomography. *Microsc Microanal,* **21**(6), 1649-1656.

Rolland, N., Vurpillot, F., Duguay, S., Mazumder, B., Speck, J.S., & Blavette, D. (2017). New Atom Probe Tomography Reconstruction Algorithm for Multilayered Samples: Beyond the Hemispherical Constraint. *Microsc Microanal,* **23**(2), 247-254.

Saad, Y. (2003). *Iterative methods for sparse linear systems* (Second ed.). Philadelphia, PA: SIAM.

Shewchuk, J.R. (1994). *An introduction to the conjugate gradient method without the agonizing pain*. Pittsburgh, PA: Carnegie-Mellon University. Department of Computer Science.

Thompson, K., Sebastian, J., & Gerstl, S. (2007). Observations of Si field evaporation. *Ultramicroscopy,* **107**(2-3), 124-130.

Tu, Y., Takamizawa, H., Han, B., Shimizu, Y., Inoue, K., Toyama, T., Yano, F., Nishida, A., & Nagai, Y. (2017). Influence of laser power on atom probe tomographic analysis of boron distribution in silicon. *Ultramicroscopy,* **173**, 58-63.

Vella, A. (2013). On the interaction of an ultra-fast laser with a nanometric tip by laser assisted atom probe tomography: A review. *Ultramicroscopy,* **132**, 5-18.

Vurpillot, F., Bostel, A., & Blavette, D. (1999). The shape of field emitters and the ion trajectories in three-dimensional atom probes. *J Microsc,* **196**, 332-336.

Vurpillot, F., Gault, B., Geiser, B.P., & Larson, D. (2013). Reconstructing atom probe data: A review. *Ultramicroscopy,* **132**, 19-30.

Vurpillot, F., Houard, J., Vella, A., & Deconihout, B. (2009). Thermal response of a field emitter subjected to ultra-fast laser illumination. *J Phys D: Appl Phys,* **42**(12), 125502.

Xu, Z., Li, D., Xu, W., Devaraj, A., Colby, R., Thevuthasan, S., Geiser, B., & Larson, D.J. (2015). Simulation of heterogeneous atom probe tip shapes evolution during field evaporation using a level set method and different evaporation models. *Comput Phys Commun,* **189**, 106-113.

Zschiesche, H., Campos, A.P.C., Dominici, C., Roussel, L., Charai, A., Mangelinck, D., & Alfonso, C. (2019). Correlated TKD/EDS - TEM - APT analysis on selected interfaces of CoSi2 thin films. *Ultramicroscopy,* **206**, 112807.

Figure captions

Figure 1.

Figure 1. Procedure of the bottom-up reconstruction method. (a) Conformal deposition of small reconstruction volume composed of three atomic layers (3 near neighbor lattices) on the known surface of an end tip. (b) Simulation to determine the evaporation rate, sequence and hit maps of the deposited atoms. (c) Bottom-up search process to find the suitable candidate atoms. Early evaporated atoms (pink, referred to as sacrificial atoms) near the surface are only used to establish the electrostatics but are not included in the reverse reconstruction (see text for a detailed description of this process). Remaining atoms (green, referred to as candidate atoms) on the tip surface define the volume that will be reconstructed. The difference in the number of pulses required to evaporate the atoms (experiment vs simulation) identifies the “missing atoms”. (d) Trajectory-matching process comparing the simulated hitting positions of the candidate atoms with experimental hit positions. Each data point is linked through the closest position on the simulated hit map with a specific candidate atom. (e) Data atoms are placed back to the lattice sites in the small reconstructed volume. Empty spaces are filled with substrate atoms. (f) Repeat steps (a) to (e) for the next volume reconstruction.

Figure 2.

Figure 2. (a) Experimental (symbol, Thompson et al. 2007) and predicted detection fluxes (line) in voltage mode for various base temperatures. (b) Predicted evaporation frequency as a function of the electric field based on the hybrid evaporation model.

Figure 3.

Figure 3. Simulated tip shapes after 800,000 atoms evaporation for (a) voltage mode and (b) laser mode. The corresponding hit maps are illustrated in (c) and (d), respectively as viewed by a very large detector (400 × 400 mm). The red circles indicate the field of view as defined by a normal detector.

Figure 4.

Figure 4. 2D slices of the evolution of simulated tips in Fig. 3 along *y*- and *x*- axes for (a) voltage mode and (b) laser mode. The gray area enclosed by the dash lines represents the region inside the field of view (assuming the diameter of the detector is 10 cm as circled in Fig. 3c and 3d).

Figure 5.

Figure 5. A (001) crystalline Si tip is evaporated in (a) voltage mode and (b) laser mode. The simulated data points lying on the hit maps within the FOV (red circle) in (c) and (d) are reconstructed to test the feasibility of reconstruction models.

Figure 6.

Figure 6. (a) A bottom-up reconstructed tip in voltage mode. Three small volumes within the entire reconstructed volume are shown with for each atom its misplacement distance highlighted by the black lines. In the majority of cases (> 91%) this is zero. (b) Trajectory-matching process: comparing the hit points of the experimental data and the simulated ones.

Figure 7.

Figure 7. (a) A bottom-up reconstructed tip in laser mode. Three small volumes within the entire reconstructed volume are shown with the distance displacement between the reconstructed atoms and their ideal positions. (b) The corresponding trajectory-matching processes.

Figure 8.

Figure 8. Position of the reconstructed atoms within the field of view of a laser evaporated tip. Calculated by using (a) the conventional reconstruction method and (b) bottom-up reconstruction method. The line segments connect the reconstructed positions with the original ones. (c) The results of the bottom-up reconstruction when adding a 50% detection efficiency. (d) Averaged displacement distance versus the reconstruction length for different reconstruction methods and detection efficiency. For the conventional method, the displacement distance (green lines) along the vertical direction Δz (tip axis) and displacement distance in the horizontal directions Δxy are outlined. For the bottom-up cases for various detection efficiency, Δd (red, blue) stays at a very low level throughout the entire reconstruction range.

Table 1

Table 1. Empirical fitting to extracted prefactors and activation energy for silicon in various evaporation mechanism based on the experimental data (Thompson et al. 2007)

	Prefactors $\nu_0\ (s^{-1})$	Activation energy $Q_b\ (eV)$
H assisted Si evaporation $\nu_{H-Si}\ (V \leq 4.5\ kV)$	$1 \times 10^{6} \cdot exp(-1.7 \times 10^{-3} \cdot V)$	$2.72 \times 10^{-1} - 2.7 \times 10^{-5} \cdot V$
Pure Si evaporation $\nu_{Si}\ (V > 4.5\ kV)$	$7 \times 10^{-13} \cdot exp(1.6 \times 10^{-2} \cdot V)$	$3.8 \times 10^{-1} + 4 \times 10^{-5} \cdot V$
Tunneling $\nu_{tunnel}\ (V\!: 2 \sim 10\ kV)$	$4.5 \times 10^{-7} \cdot exp(1.17 \times 10^{-3} \cdot V)$	$5 \times 10^{-7} \cdot V$

Figure 1

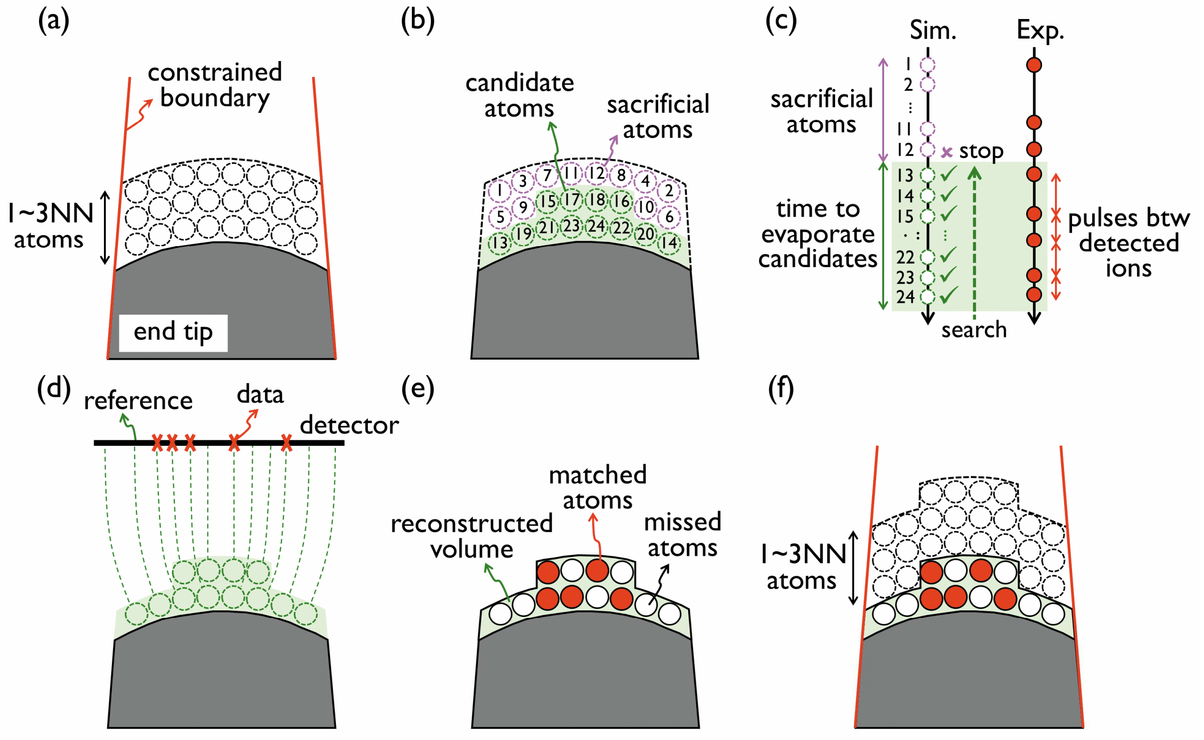
(a)
constrained boundary
1~3NN atoms
end tip
(b)
candidate atoms
sacrificial atoms
1 3 7 11 12 8 4 2
5 9 15 17 18 16 10 6
13 19 21 23 24 22 20 14
(c)
Sim.
Exp.
sacrificial atoms
1
2
11
12
stop
time to evaporate candidates
13
14
15
22
23
24
search
pulses btw detected ions
(d)
reference
data
detector
(e)
matched atoms
reconstructed volume
missed atoms
(f)
1~3NN atoms

Figure 2

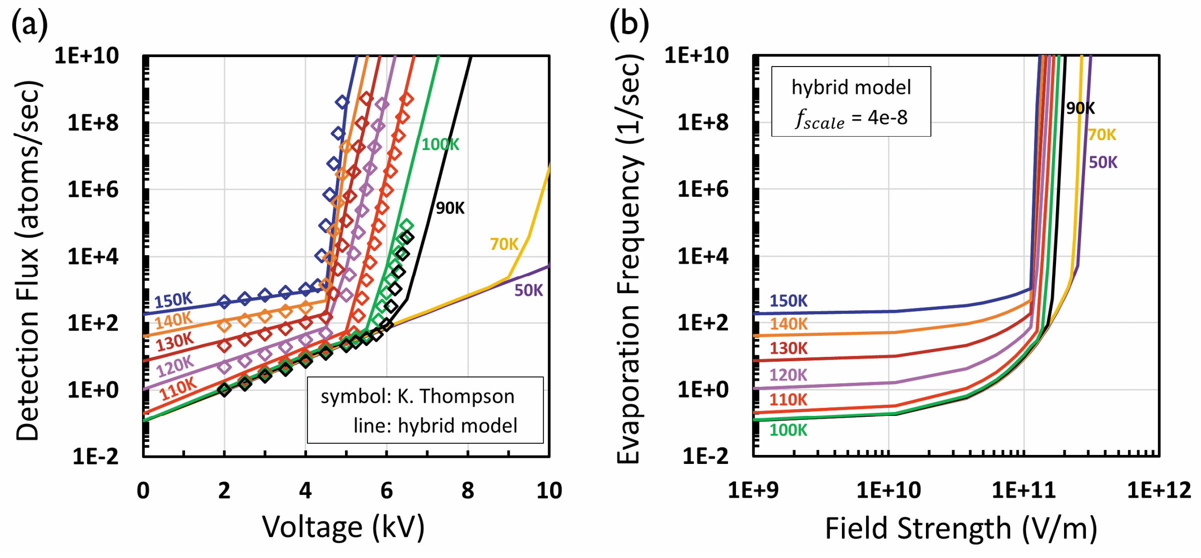
(a)
Detection Flux (atoms/sec)
1E+10
1E+8
1E+6
1E+4
1E+2
1E+0
1E-2
0
2
4
6
8
10
Voltage (kV)
150K
140K
130K
120K
110K
100K
90K
70K
50K
symbol: K. Thompson
line: hybrid model
(b)
Evaporation Frequency (1/sec)
1E+10
1E+8
1E+6
1E+4
1E+2
1E+0
1E-2
1E+9
1E+10
1E+11
1E+12
Field Strength (V/m)
hybrid model
f_{scale} = 4e-8
90K
70K
50K
150K
140K
130K
120K
110K
100K

Figure 3

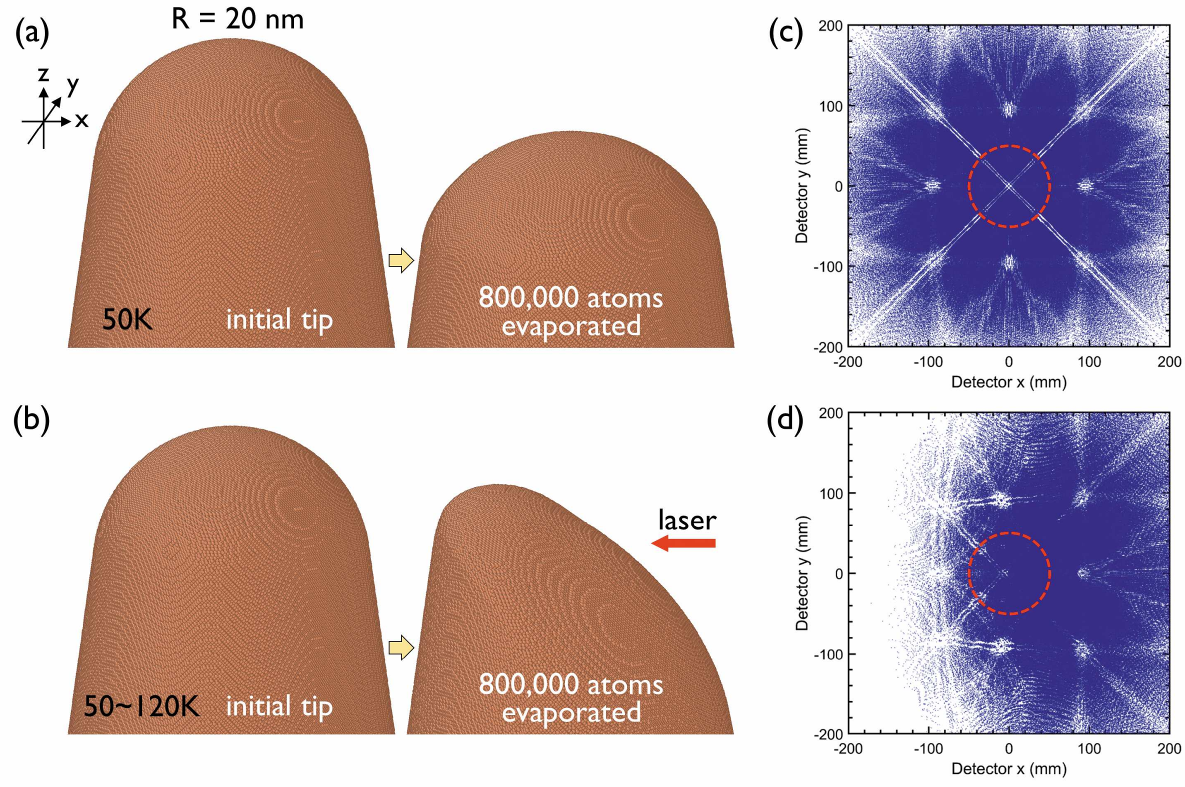
(a)
R = 20 nm
z
y
x
50K
initial tip
800,000 atoms evaporated
(b)
50~120K
initial tip
800,000 atoms evaporated
laser
(c)
Detector y (mm)
Detector x (mm)
200
100
0
-100
-200
-200
-100
0
100
200
(d)
Detector y (mm)
Detector x (mm)
200
100
0
-100
-200
-200
-100
0
100
200

Figure 4

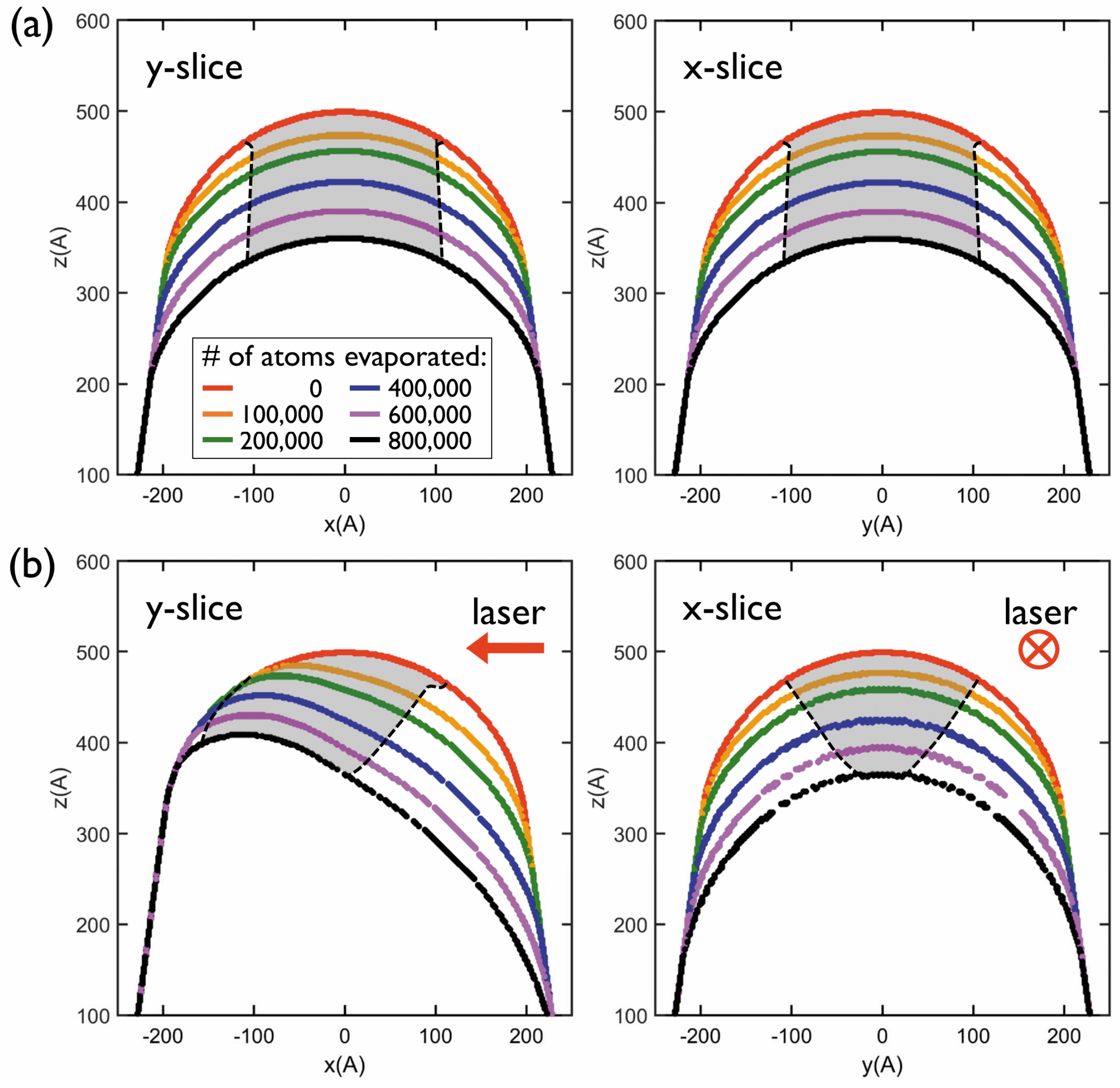
(a)
y-slice
x-slice
# of atoms evaporated:
0
100,000
200,000
400,000
600,000
800,000
z(A)
x(A)
y(A)
600
500
400
300
200
100
-200
-100
0
100
200
(b)
y-slice
laser
x-slice
laser

Figure 5

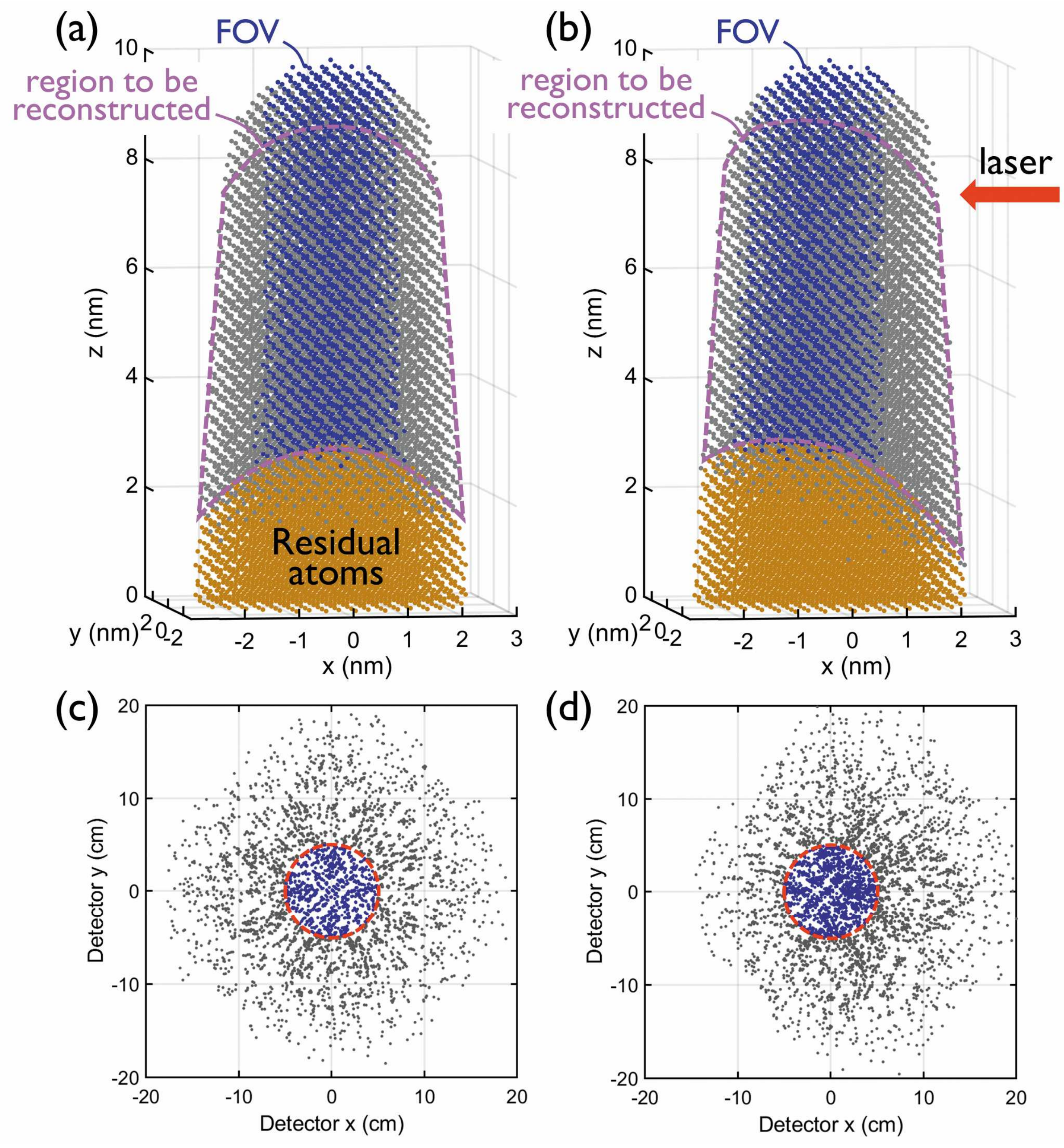
(a)
FOV
region to be reconstructed
Residual atoms
z (nm)
y (nm)
x (nm)
(b)
FOV
region to be reconstructed
laser
z (nm)
y (nm)
x (nm)
(c)
Detector y (cm)
Detector x (cm)
(d)
Detector y (cm)
Detector x (cm)

Figure 6

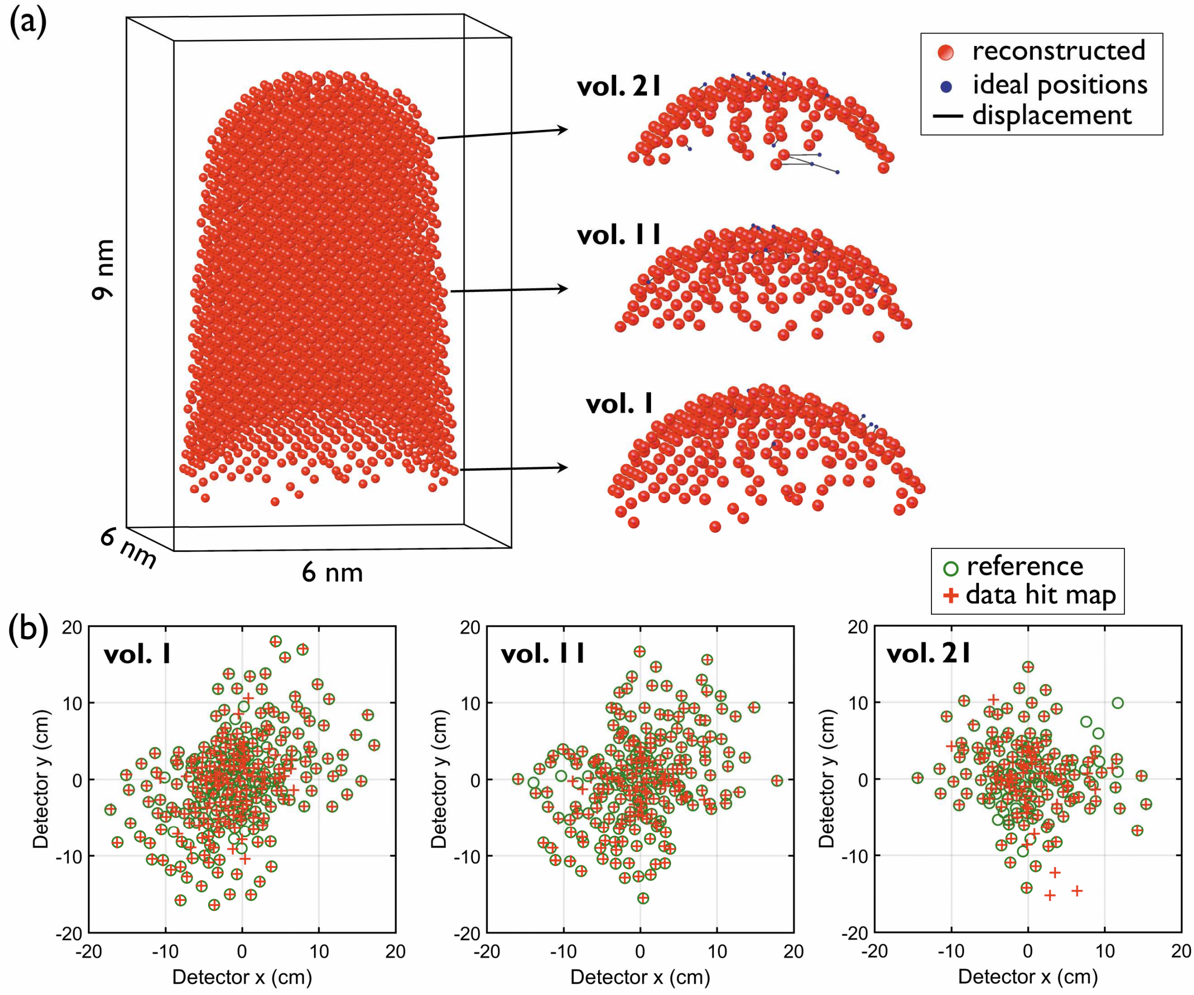
(a)
9 nm
6 nm
6 nm
vol. 21
vol. 11
vol. 1
reconstructed
ideal positions
displacement
(b)
reference
data hit map
vol. 1
vol. 11
vol. 21
Detector y (cm)
Detector x (cm)
20
10
0
-10
-20
-20
-10
0
10
20

Figure 7

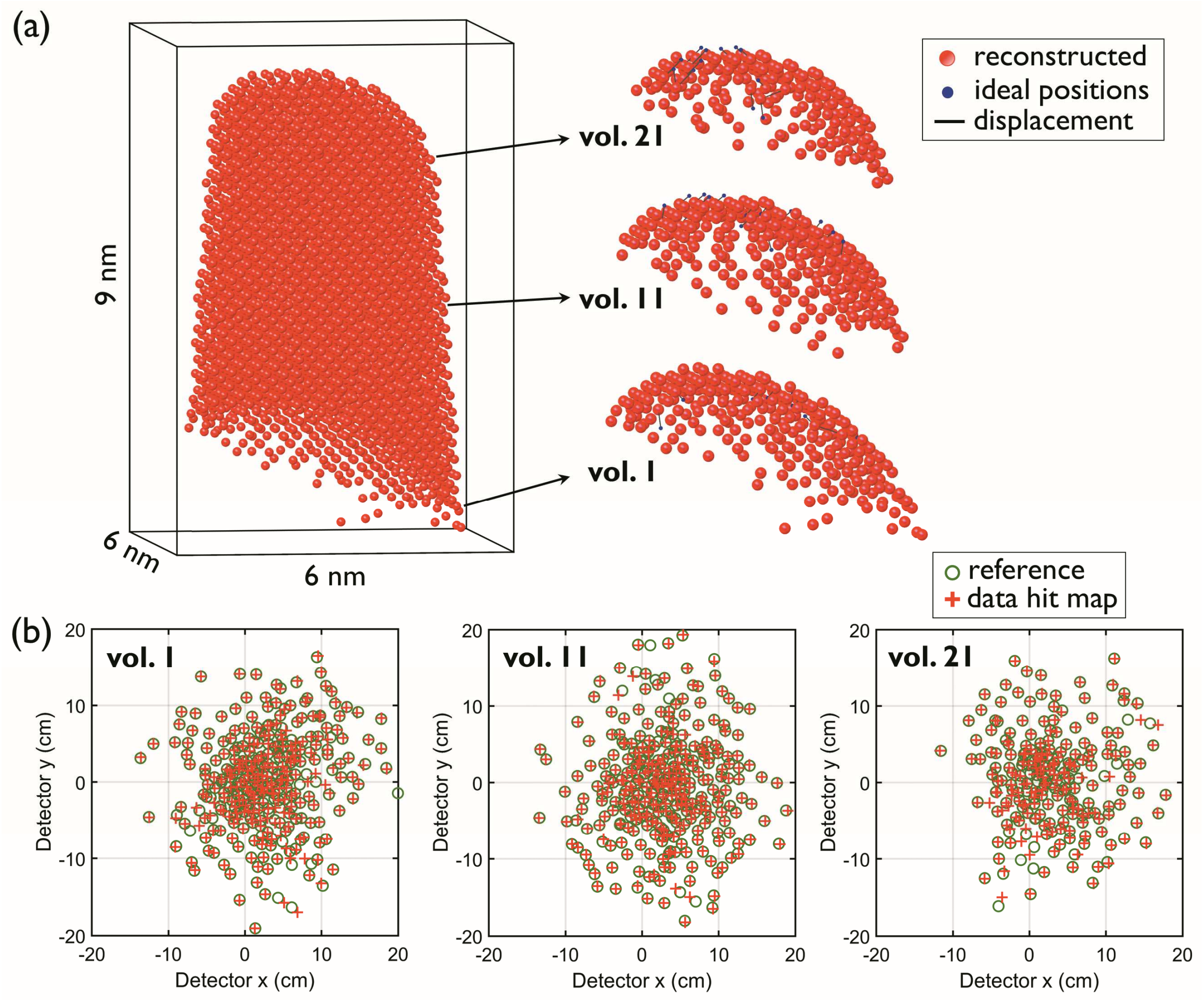
(a)
9 nm
6 nm
6 nm
vol. 21
vol. 11
vol. 1
reconstructed
ideal positions
displacement
reference
data hit map
(b)
vol. 1
vol. 11
vol. 21
Detector y (cm)
Detector x (cm)
20
10
0
-10
-20
-20
-10
0
10
20

Figure 8

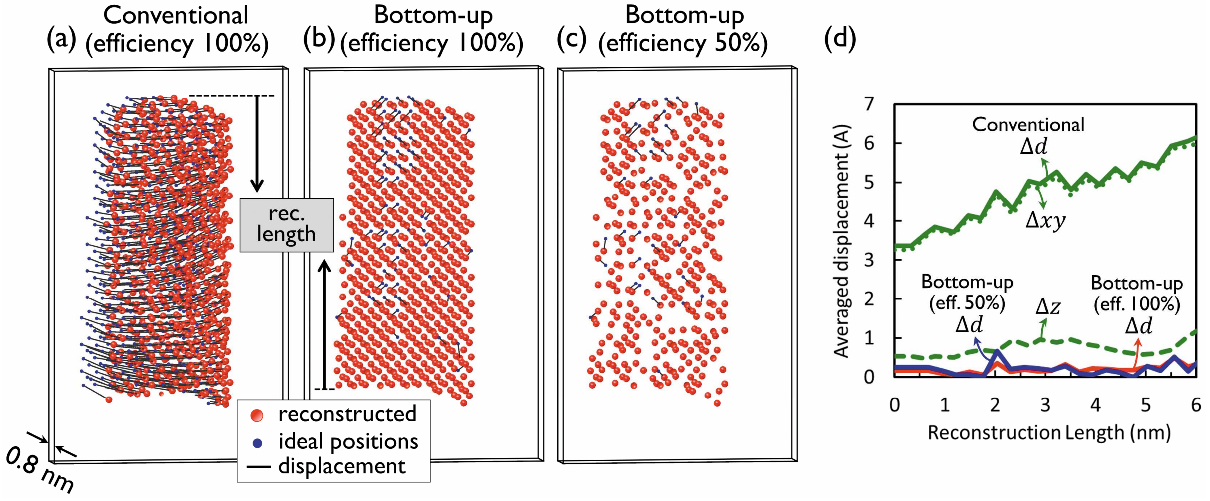
(a) Conventional (efficiency 100%)
(b) Bottom-up (efficiency 100%)
(c) Bottom-up (efficiency 50%)
(d)
rec. length
0.8 nm
reconstructed
ideal positions
displacement
Averaged displacement (A)
Reconstruction Length (nm)
0
1
2
3
4
5
6
7
Conventional
Δd
Δxy
Bottom-up (eff. 50%)
Δd
Δz
Bottom-up (eff. 100%)
Δd